Ignition and combustion characteristics of micron-sized Al-Li alloy particle in high-temperature gas flow

Zhenkun Hu [a], Shengyu Pang [a], Yugan Liao [a], Yong Tang [a], Qian Mao [a], Baolu Shi [a,b,*]

[a] School of Aerospace Engineering, Beijing Institute of Technology, Beijing 100081, PR China
[b] Chongqing Innovation Center, Beijing Institute of Technology, Chongqing 404100, PR China

ARTICLE INFO

ABSTRACT

Compared to pure aluminum particles, Al-Li alloy particles exhibit shorter ignition delay times and smaller combustion product sizes, making them a superior metallic additive for solid propellants. Therefore, this study experimentally and theoretically investigated the ignition and combustion characteristics of micron-sized Al-Li alloy particle. First, the ignition delay times of 8 μm Al-Li alloy particle over a wide range of temperatures were measured using a reflected shock tube. Second, theoretical models of ignition and combustion of micron-sized Al-Li alloy particle in high-temperature gas flow were developed, by considering comprehensive processes including convective heat transfer, radiative heat transfer, heterogeneous surface reactions, phase change, oxide layer rupture, diffusion-controlled combustion and micro-explosion. The ignition delay times and critical ignition temperature predicted by the model show good agreement with the experimental results. Detailed analysis reveals that micro-explosion can occur as the saturation vapor pressure of lithium exceeds the contact pressure at the Al-Li interface during combustion. Parametric studies further indicate that elevating ambient pressure increases the contact pressure at the Al-Li interface, thereby inhibiting micro-explosion. In contrast, raising ambient temperature increases the saturation vapor pressure of lithium, thus facilitating micro-explosion. Finally, an empirical formula was derived to predict the critical ambient pressure at which micro-explosion occurs in Al-Li alloy particle with 5 % lithium content.

Novelty and Significance Statement: In this study, both the ignition delay times and the critical ignition temperature of Al-Li alloy particle were measured using a reflected shock tube. Subsequently, theoretical models of ignition and combustion of micron-sized Al-Li alloy particle in high-temperature gas flow were developed, encompassing convective heat transfer, radiative heat transfer, heterogeneous surface reactions, phase change, oxide layer rupture, diffusion-controlled combustion and micro-explosion. Based on the model, the heat and mass transfer mechanism of Al-Li alloy particle during ignition and combustion was revealed, and particularly elucidating the micro-explosion mechanism as well as the effects of ambient pressure and temperature on micro-explosion. Finally, an empirical formula was proposed to predict the critical ambient pressure at which micro-explosion occurs in Al-Li alloy particle.

1. Introduction

Aluminum powder is a commonly utilized metallic fuel for solid rocket motors (SRM), primarily due to its high volumetric heat value [1]. The heat generated during its combustion can dramatically raise the combustion chamber temperature, thereby increasing the specific impulse. However, molten aluminum particles are highly prone to agglomeration near the propellant burning surface, leading to the formation of large particles [2]. Upon discharge through the nozzle, these large particles exhibit considerable lag in velocity and temperature

compared to the gas, resulting in notable two-phase flow losses. Generally, the unbalanced flow between phases results in a loss of specific impulse ranging from 1.5 % to 2 %, with a maximum of 5 % [3], severely hindering the improvement of SRM's actual specific impulse. To address this issue, using aluminum-based binary alloys instead of micron aluminum powders to reduce the size of condensed-phase products has been demonstrated as a potential solution [4–6]. Among these alloys, aluminum-lithium (Al-Li) alloy particles have attracted extensive attention owing to their advantages [7].

The addition of lithium with high metallic activity to aluminum

particles results in alterations in the structure and strength of the oxide layer, facilitating the rupture of the oxide layer at elevated temperatures and thereby enhancing the reactivity of the alloy particles [8,9]. Consequently, Al-Li alloy particles ignite more easily compared to pure aluminum [10,11], with critical ignition temperatures (1000–1400 K) that are significantly lower than those of aluminum particles (1700–2300 K) [12]. Furthermore, the significant difference in boiling points between aluminum and lithium may result in the vaporization of lithium within alloy particles. The large expansion pressure generated by this vaporization would induce micro-explosion [7], effectively fragmenting the condensed-phase products and thus reducing two-phase flow losses. On the other hand, lithium can reduce the average molecular weight of the gas-phase products due to its low molar mass (6.94 g/mol), which also contributes to increasing the specific impulse [13]. In addition, substituting Al-Li alloy particles for aluminum powder in ammonium perchlorate composite propellant (APCP) can markedly diminish the concentration of HCl in the combustion products [14], thereby reducing environmental pollution and inhibiting the formation of secondary smoke in the exhaust plume of SRM.

In view of the aforementioned advantages, the ignition and combustion characteristics of Al-Li alloy particles and their potential applications in solid propellants have been extensively studied. Xu et al. [15] conducted laser-induced ignition experiments on individual Al-Li alloy particle and found that the oxide layer of the alloy particle facilitated oxygen diffusion more effectively than that of pure aluminum particle, thereby significantly shortening the ignition delay time. Employing differential scanning calorimetry and thermogravimetric analysis methodologies, Zhou et al. [16] investigated the thermal oxidation behavior of Al-Li alloy particles. The results demonstrated that an increase in lithium content reduced the activation energy for the oxidation reaction of the alloy particles, which in turn lowered both the critical ignition temperature and the ignition delay time. The shortened ignition delay time reduced the particle residence time on the propellant burning surface, thereby decreasing the particle number density. This resulted in a significant decline in agglomerate size [2], consistent with the experimental phenomenon observed by Xiong et al. [17]. Terry et al. [18,19] experimentally and theoretically investigated the micro-explosion phenomena near the propellant burning surface using 80/20 wt. % Al-Li alloy particles as a metal fuel for APCP. Their analysis indicated that the micro-explosion was caused by the molten particle's Lewis number being much greater than 1, which led to volatile lithium overheating before it could diffuse to the particle surface. Furthermore, thermodynamic calculations revealed that using Al-Li alloy particles with lithium content exceeding 15 % reduced HCl production by over 95 % and improved the theoretical specific impulse by 7 s compared to pure aluminum.

In order to investigate the influence of ambient pressure on the micro-explosion of Al-Li alloy particles, Diez et al. [5] measured the burning rate of Al-Li based composite propellants under various pressure conditions. The results indicated that the pressure index of the propellant burning rate was 0.59 at pressures below 4 MPa, and it decreased to 0.11 at pressures exceeding 4 MPa. The authors concluded that the pressure sensitivity of the burning rate was reduced at elevated pressures, which they attributed to the inhibition of micro-explosion in Al-Li alloy particles or enhanced condensed-phase reactions on the propellant burning surface. In contrast, Xu et al. [20] experimentally investigated the combustion characteristics of individual micron-sized Al-Li alloy particle at pressures ranging from 0.1 to 0.8 MPa and found that the combustion temperature of the alloy particle decreased with increasing pressure. They concluded that Al-Li alloy particle was more prone to undergoing micro-explosion at high pressures. The micro-explosive behaviors observed by Diez et al. [5] and Xu et al. [20] seemed contradictory, and hence understanding the micro-explosive mechanism is indispensable to clarify such phenomenon.

In summary, Al-Li alloy particles have advantages over pure aluminum particles in terms of the shorter ignition delay time and the smaller agglomerate size, as well as the reduced HCl content in the combustion products, which makes them the optimal metal additives for solid propellants. Nevertheless, solid propellants are typically employed in high-pressure environments (generally beyond 7 MPa). Although the ignition and combustion process of Al-Li alloy particles in propellant combustion environments have been preliminarily investigated, the mechanism through which ambient pressure influences the ignition, combustion, and micro-explosion of Al-Li alloy particles remains unclear. Therefore, the development of a theoretical model that elucidates the ignition and combustion process of individual Al-Li alloy particle is of paramount importance. This will facilitate a comprehensive analysis of the ignition, combustion, and micro-explosion characteristics of Al-Li alloy particle across a wide range of pressures.

The rest of this study is organized through the following frame. Firstly, the ignition delay times of Al-Li alloy particle over a wide temperature range were measured in a reflected shock tube. Secondly, theoretical models for the ignition and combustion of micron-sized Al-Li alloy particle in high-temperature gas flow were developed and validated using the experimentally measured ignition delay times and critical ignition temperature. Finally, the ignition and combustion characteristics of Al-Li alloy particle were analyzed in detail, and the effects of ambient pressure and temperature on micro-explosion behavior were investigated.
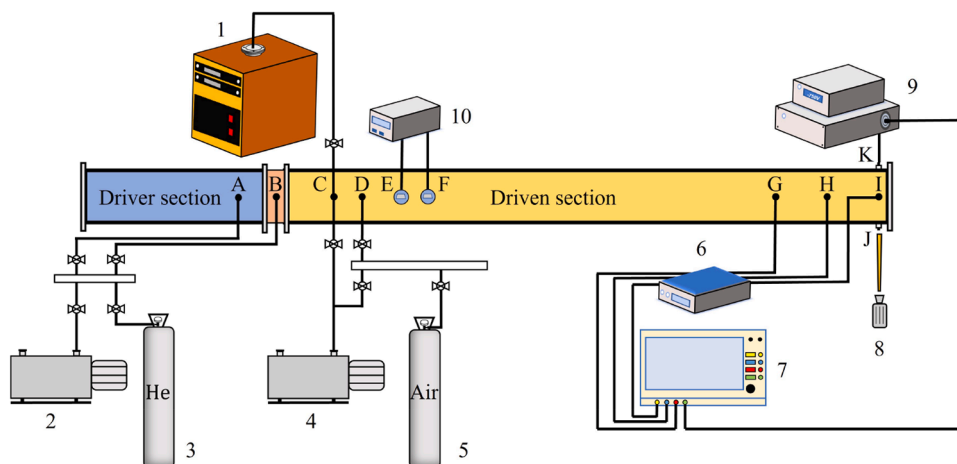
2. Experimental

2.1. Experimental setup

The experiment was conducted using the reflected shock tube platform illustrated in Fig. 1. The tube has a total length of 13.1 m, consisting of a 3-m driving section, a 10-m driven section, and a 0.2-m double-diaphragm section. After evacuating the shock tube to its ultimate vacuum, the leakage rate was measured at 0.2 kPa/min, with shock wave attenuation remaining below 5 %, both of which met the experimental requirements. The platform is equipped with mechanical pumps, a molecular pump (KYKY-FJ1300-F), high-precision digital pressure gauges, and a vacuum gauge (INFCON CDG025D). This vacuum gauge features two accuracy levels and monitors the pressure of both the driving gas and the test gas. Two coaxial circular optical windows (8 mm in diameter) are mounted radially 20 mm above the base of the driven section. One window is coupled via optical fibers to a photomultiplier tube and monochromator, while the other allows observation of the ignition and combustion characteristics of Al-Li alloy particles using a DSLR camera. The monochromator offers a mechanical scanning range of 0–1200 nm and achieves a spectral resolution of 0.05 nm. Three pressure sensors (PCB 113B27) are installed at 0.5-m intervals along the end of the driven section and connected to a signal conditioner (PCB 482C16). Both the sensors and the monochromator are interfaced with a four-channel oscilloscope (Tektronix MDO3), which has a sampling rate of 2.5 GS/s. This setup enables synchronous recording of pressure and selected spectral signals throughout the experiment.

2.2. Experimental methods

In the experiment, Al-Li alloy particles with an average diameter of 8 μm (±2 μm) and 5 % lithium content were used. The microscopic morphology and size distribution of the Al-Li alloy particles are shown in Fig. 2. The particles exhibit good sphericity, but with noticeable surface roughness, which may be attributed to the uneven adhesion of lithium elements on the particle surface during the preparation process. The particle size distribution appears relatively monodisperse, with a median particle size (D50) of 7.25 μm. The X-Ray Diffraction (XRD) spectrum in Fig. 3 shows that the sample only exhibits the typical diffraction peaks of Al, without characteristic peaks of metallic lithium detected. This is primarily attributed to the low lithium content in the alloy particles. To confirm the existence of lithium, quantitative analysis using

Fig. 1. Schematic of experimental setup. A - High-pressure section inlet/exhaust port. B - Double-diaphragm section inlet/exhaust port. C - Low-pressure section exhaust port. D - Low-pressure section inlet port. E - Low-Precision Vacuum Gauge. F - High-Precision Vacuum Gauge. G, H, I - Pressure Sensors. J, K - Optical Windows. 1 - Molecular Pump. 2 - Driving Section Mechanical Pump. 3 - Driving Section Gas. 4 - Driven Section Mechanical Pump. 5 - Driven Section Gas. 6 - Signal Amplifier. 7 - Oscilloscope. 8 - DSLR Camera. 9 - Monochromator. 10 - Vacuum Gauge.
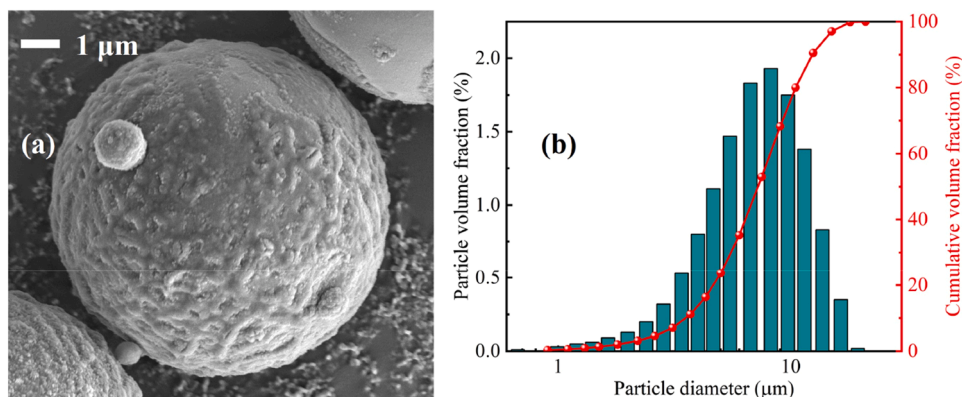
Fig. 2. SEM image and size distribution of the Al-Li alloy particles.
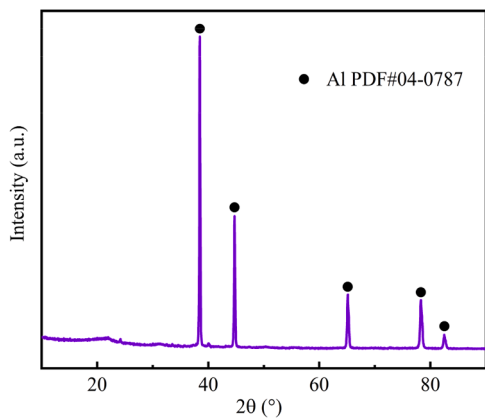
Fig. 3. XRD spectrum of the Al-Li alloy particles.

inductively coupled plasma optical emission spectroscopy (ICP-OES) was performed, and the measured lithium content was 4.8 %.

Before the experiment, a stainless-steel stanchion fitted with a thin blade was rigidly mounted on the end cap, and 2–4 mg of alloy powder was uniformly distributed on the blade surface. During the evacuation of the driven section, the pressure drop rate was maintained below 1 kPa/s to prevent premature dislodging of the powder prior to diaphragm

rupture. Helium served as the driver gas in the driving section, and dry air was used as the test gas in the driven section. Following full pressurization of the driven section, the driving section and double-diaphragm section were simultaneously filled. The diaphragm rupture experiment was triggered when the gas pressure reached the preset threshold.

Upon diaphragm rupture, the high-pressure gas rapidly compressed the low-pressure gas, generating an incident shock wave. As the shock wave propagated past the blade, the alloy powder was fluidized and dispersed. The shock wave then reflected from the end cap, and the resulting reflected wave instantaneously heated the Al-Li particles to the target temperature, initiating ignition and combustion. Simultaneously, the emission spectral signal of AlO was transmitted through an optical fiber to the monochromator's entrance slit, converted to an electrical signal by a photomultiplier tube, and recorded by the oscilloscope. In this study, the ignition delay time of Al-Li alloy particles is defined as the time interval beginning when the driven section attains the pressure in region 5 (the region behind the reflected shock) and ending when the AlO spectral signal reaches half of its first peak, as depicted in Fig. 4. The blue curve depicts the pressure profile in region 5, and the red curve corresponds to the AlO emission spectrum during combustion.

3. Modeling

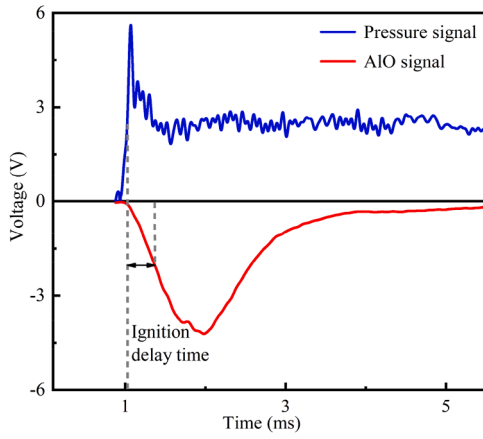This study focuses on a single micron-sized Al-Li alloy particle, which

Fig. 4. Schematic for determining the ignition delay time of Al-Li alloy particle.

is composed of an aluminum core and an oxide layer, with lithium uniformly dispersed throughout the aluminum core. According to Zhu et al.'s study on Al-Li alloy particles with lithium contents ranging from 3 % to 10 % [7], the characteristic diffraction peaks of the AlLi inter-metallic compound begin to appear when lithium content reaches 7 %, suggesting that the maximum solid solubility of lithium in aluminum is approximately 5 %. Consequently, the presence of intermetallic compounds in alloy particle with lithium content below 5 % can be neglected. As depicted in Fig. 5(a), the alloy particle is exposed to a hot oxidizing gas flow environment, where heat is transferred to it via convection and radiation. As the particle temperature (T_p) increases, T_p first reaches the melting point of lithium (453.69 K), causing the lithium to undergo a phase transition from solid to liquid, as illustrated in Fig. 5 (b). Subsequently, as T_p continues to rise, it reaches the melting point of aluminum (933.45 K), triggering the melting of aluminum core. The oxidizing gases diffuse through the oxide layer and reach the surface of the aluminum core, where they undergo chemical reactions with both aluminum and lithium.

The molecular dynamics simulations conducted by Zhou et al. [21] revealed that during the heating process, the increase in kinetic energy of metal atoms significantly enhances lithium diffusion. However, the oxide layer acts as a diffusion barrier, hindering the outward migration of lithium. As a result, lithium atoms progressively migrate inward, forming a lithium-rich core. Eventually, the alloy particle is divided into two parts: a central lithium cluster and an outer shell. Therefore, it is assumed that after the complete melting of aluminum, lithium precipitates out of the molten core and forms a spherical droplet within the

resulting structure, as shown in Fig. 5(c). In addition, the volume expansion of lithium and aluminum is significantly greater than that of the oxide layer, resulting in the generation of expansion stress at the interface between the aluminum core and the oxide layer. When the expansion stress exceeds the critical stress of the oxide layer, the oxide layer ruptures, releasing the heterogeneous surface reactions from its constraint, and prompting a rapid rise in T_p.

In the present model, ignition is considered successful when T_p reaches the melting point of alumina (2327 K) and the duration required for T_p to increase from 298 to 2327 K is defined as the ignition delay time. For a 100-μm Al-Li alloy particle with 5 % lithium content in the 2000 K air environment, the thermal conductivity of the gas is 0.105 W/(m•K), while that of the particle is 195 W/(m•K)[22,23]. Assuming a Nusselt number of 2, the calculated Biot number is 1.8×10^{-4}, which is several orders of magnitude lower than unity. Therefore, the lumped parameter method is employed to analyze the ignition process. Accordingly, the energy equation can be expressed as

$$m_p c_{p,p} \frac{dT_p}{dt} = \dot{Q}_{conv} + \dot{Q}_{rad} + \dot{Q}_{hsr} - \dot{Q}_{melt} \tag{1}$$

where m_p and $c_{p,p}$ are the mass and specific heat capacity of the alloy particle, respectively. $\dot{Q}_{conv}$ and $\dot{Q}_{rad}$ account for the convection and radiation rates, respectively. $\dot{Q}_{hsr}$ represents the heat release rate of the surface reaction, and $\dot{Q}_{melt}$ is the heat absorption rate during the melting period. It is assumed that T_p always remains at the melting point during the melting period.

Furthermore, due to the discrepancy in thermal expansion coefficients between aluminum and lithium, contact pressure is generated at the interface between the aluminum core and the lithium droplet during the heating process. If the contact pressure consistently remains greater than the saturation vapor pressure of lithium, the alloy particle will proceed into the quasi-steady combustion stage as illustrated in Fig. 5(d). During this stage, aluminum vapor escapes from the exposed surface of the aluminum core and reacts with surrounding oxidizers, forming a diffusion flame above the aluminum core. Additionally, nanoscale oxide particles produced by gas-phase reactions diffuse to both sides of the flame. Oxide particles that diffuse inwardly deposit on the surface of the droplet, resulting in the growth of an oxide cap. If the contact pressure drops to the saturation vapor pressure of lithium, the lithium droplet undergoes instantaneous vaporization. The rapid volume expansion resulting from this vaporization leads to the fragmentation of the alloy particle, a phenomenon known as micro-explosion, as depicted in Fig. 5(e). The time period from the initial state of the alloy particle to the onset of micro-explosion is defined as the micro-explosion delay time.
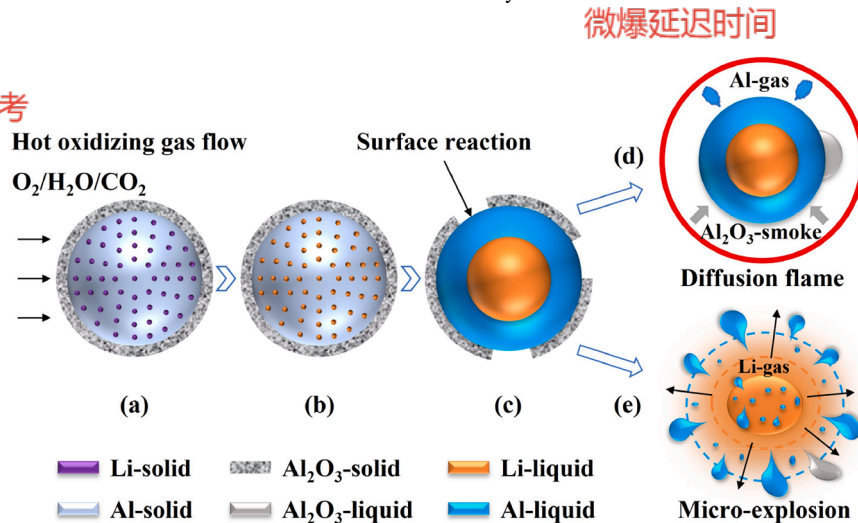

Fig. 5. Schematic of the ignition and combustion process of Al-Li alloy particle.

In summary, the ignition and combustion of Al-Li alloy particle in a hot oxidizing gas flow encompass multiple physicochemical processes, primarily including gas-particle heat transfer, heterogeneous surface reactions, oxide layer rupture, vapor-phase combustion, and micro-explosion. Herein, corresponding theoretical models are established to elucidate the underlying mechanisms of ignition, combustion, and micro-explosion of Al-Li alloy particle.

3.1. Gas-particle heat transfer

During the ignition stage, heat is transferred to the alloy particle from the surrounding high-temperature gas flow through convection and radiation. The convective heat transfer rate is given as

$$\dot{Q}_{conv} = \pi d_p \lambda_g Nu_p \left(T_a - T_p \right) \tag{2}$$

where λ_g and T_a represent the thermal conductivity and temperature of the gas flow, respectively. d_p denotes the particle diameter, and Nu_p is the Nusselt number that can be calculated from the Ranz-Marshall model [24] as

$$Nu_p = 2 + 0.6 Re_p^{1/2} Pr_g^{1/3} \tag{3}$$

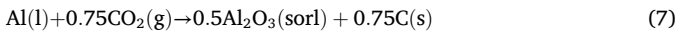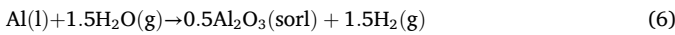where Re_p and Pr_g are the Reynolds number and Prandtl number, respectively.

It is assumed that the gas flow surrounding the particle is an infinitely large cavity with a temperature of T_a. The radiative heat transfer between the particle and the inner surface of the cavity is governed by the Stefan-Boltzmann law as

$$\dot{Q}_{rad} = \varepsilon_p A_p \sigma \left(T_a^4 - T_p^4 \right) \tag{4}$$
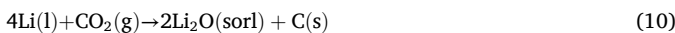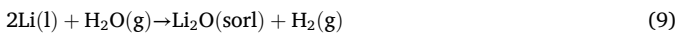
where $\varepsilon_p = 0.3$ [25] is the particle emissivity, and $\sigma = 5.67 \times 10^{-8}$ W/(m$^2 \cdot$ K^4) is the Stefan-Boltzmann constant.

3.2. Heterogeneous surface reactions

Three global heterogeneous surface reactions between aluminum and oxidizers [26] are considered in the present study, i.e.,

$$Al(l) + 0.75 O_2(g) \rightarrow 0.5 Al_2O_3(sorl) \tag{5}$$

$$Al(l) + 1.5 H_2O(g) \rightarrow 0.5 Al_2O_3(sorl) + 1.5 H_2(g) \tag{6}$$

$$Al(l) + 0.75 CO_2(g) \rightarrow 0.5 Al_2O_3(sorl) + 0.75 C(s) \tag{7}$$

Among the lithium oxides, Li_2CO_3 and $LiOH$ are susceptible to decomposition at high temperatures, whereas Li_2O is relatively stable [27]. Consequently, the following global heterogeneous surface reactions between lithium and oxidizers are employed in the present study, as detailed below:

$$2Li(l) + 0.5 O_2(g) \rightarrow Li_2O(sorl) \tag{8}$$

$$2Li(l) + H_2O(g) \rightarrow Li_2O(sorl) + H_2(g) \tag{9}$$

$$4Li(l) + CO_2(g) \rightarrow 2Li_2O(sorl) + C(s) \tag{10}$$

In the case of surface reactions controlled by chemical kinetics, the reaction rates presented in Eqs. (5)-(7) are calculated according to the following equation proposed by Gurevich et al. [28] and Mohan et al. [29], respectively:

$$\dot{m}_{Kin,ox} = \begin{cases} A_{eff} \rho_{g,s} Y_{ox,s} A_r \exp\left(-\dfrac{E_a}{R_u T_p} \right), ox = O_2 \, or \, H_2O \\ A_{eff} p_{ox,s} A_r \exp\left(-\dfrac{E_a}{R_u T_p} \right), ox = CO_2 \end{cases} \tag{11}$$

where $\dot{m}_{Kin,ox}$ is the kinetically controlled rate of aluminum

consumption, A_{eff} is the effective surface area of the alloy particle, $R_u = 8314.5$ J/(kmol·K) is the universal gas constant, and $\rho_{g,s}$ is the gas density. $Y_{ox,s}$ and p_{ox} are the mass fraction and partial pressure of the oxidizer near the particle surface, respectively.

In the case of surface reactions controlled by diffusion, a simple oxidizer diffusion model proposed by Mi et al. [30] is employed for calculating the reaction rates presented in Eqs. (5)-(7) in the present study as follows:

$$\dot{m}_{Diff,ox} = A_{eff} \frac{Sh \rho_{g,s} D_{ox}}{d_{Al}} \left(Y_{ox,\infty} - Y_{ox,s} \right) / \kappa_{st,ox} \tag{12}$$

where $\dot{m}_{Diff,ox}$ is the diffusion-controlled rate of aluminum consumption. D_{ox} is the diffusion coefficient of the oxidizer. $Y_{ox,\infty}$ is the mass fraction of the oxidizer in the ambient, and $\kappa_{st,ox}$ is the mass stoichiometric for different oxidizers. Sh is the Sherwood number, and for a spherical particle, it can be calculated by the Frössling correlation as

$$Sh = 2 + 0.552 Re_p^{1/2} Sc^{1/3} \tag{13}$$

where Sc is the Schmidt number.

In the reactions represented by Eqs. (8)-(10), during the aluminum melting stage, the lithium is uniformly dispersed in the aluminum core, resulting in the consumption rate ratio of lithium to aluminum equivalent to the mass fraction of lithium. Upon complete melting of the aluminum, it is presumed that the lithium is fully encapsulated within the aluminum core and does not participate in any reactions according to the current model.

It is assumed that the effective surface area of the alloy particle is proportional to the expansion percentage of the aluminum core and can be expressed as

$$A_{eff,1} = 4\pi \psi r_{Al,0}^2 = 4\pi \left(r_{Al}^2 - r_{Al,0}^2 \right) \tag{14}$$

where ψ and r_{Al} denote the expansion percentage and radius of the aluminum core, respectively. The subscript 0 represents the initial value.

Furthermore, the hindrance effect of newly formed alumina and lithium oxide on oxidizer diffusion also needs to be considered. Before the oxide layer ruptures, it is reasonable to assume that the effective surface area of the alloy particle is inversely proportional to the thickness of the newly formed oxide layer. Accordingly, the effective surface area can be calculated by

$$A_{eff,2} = 4\pi \psi r_{Al,0}^2 \frac{\delta_0}{\delta_0 + \delta_{new}} \tag{15}$$

where δ_{new} is the thickness of the newly formed oxide layer.

Finally, the heat release rate of the surface reactions is calculated as

$$\dot{Q}_{hsr} = \sum_{ox} \left(\dot{m}_{Al,ox} h_{Al,ox} + \dot{m}_{Li,ox} h_{Li,ox} \right), ox = O_2, H_2O \, and \, CO_2 \tag{16}$$

where $\dot{m}_{Al,ox}$ and $\dot{m}_{Li,ox}$ are the consumption rates of aluminum and lithium, respectively. $h_{Al,ox}$ and $h_{Li,ox}$ account for the heat released by the surface reactions for aluminum and lithium, respectively.

3.3. Oxide layer rupture

The critical stress of the oxide layer obtained based on Griffith's theory [31] is given as

$$\sigma_{crit,\,0} = \frac{K_c}{\sqrt{\pi a_{crit}}} \tag{17}$$

where $K_c = 3.5$ MPa•m$^{1/2}$ represents the fracture toughness of the oxide layer, and a_{crit} is the characteristic size of the microcracks existing in the oxide layer, which is comparable to the interplanar distance in the crystal lattice of alumina [31]. The oxide layer ruptures when its equivalent stress exceeds the critical stress.

Lee et al. [8] demonstrated that incorporating lithium with high metal activity into aluminum particle alters the structure of the oxide layer, while facilitating the rupture of the oxide layer at elevated temperatures. Consequently, as the lithium content in Al-Li alloy particle increases, the critical stress of the oxide layer decreases. Assuming that the critical stress varies linearly with the lithium content, it can be represented as

$$\sigma_{\mathrm{crit}} = (1 - Y_{\mathrm{Li}})\sigma_{\mathrm{crit},0} \tag{18}$$

where Y_{Li} is the mass fraction of lithium in alloy particle.

3.4. Micro-explosion

By analyzing the micro-explosion phenomenon in water-fuel emulsion droplet, Sazhin et al. [32] discovered that when the temperature at the water-fuel interface reaches the boiling point of water, the rapid evaporation of water causes the emulsion droplet to expand, leading to micro-explosion. Similarly, in Al-Li alloy particle, rapid vaporization of liquid lithium occurs when its saturation vapor pressure exceeds the contact pressure at the Al-Li interface, resulting in micro-explosion. Consequently, the condition for triggering such micro-explosion can be expressed as

$$P_{\mathrm{sat}} \geq P_{\mathrm{L}} \tag{19}$$

where P_{sat} and P_{L} denote the saturation vapor pressure of lithium and the contact pressure at the Al-Li interface, respectively.

The saturation vapor pressure of lithium as a function of temperature can be calculated by the Clausius-Clapeyron equation as

$$\frac{\mathrm{d}P_{\mathrm{sat}}}{P_{\mathrm{sat}}} = \frac{h_{\mathrm{fg}}}{R}\frac{\mathrm{d}T_{\mathrm{sat}}}{T_{\mathrm{sat}}^2} \tag{20}$$

where h_{fg} is the latent heat of evaporation, T_{sat} represents the saturation temperature, and R accounts for the gas constant.

3.5. Contact pressure in the particle

The linear thermal expansion coefficients for lithium, aluminum and alumina at $T_{\mathrm{p}} = 298$ K are 4.0×10^{-5}, 2.3×10^{-5} and 4.6×10^{-6} K^{-1}, respectively [33–35]. The discrepancy in these coefficients results in the generation of contact pressures among the different components within the alloy particle as T_{p} increases, as shown in Fig. 6(a). The method for calculating the contact pressures at the Al-Alumina interface and Al-Li interface is presented next. As illustrated in Fig. 6(b), the shell has an inner diameter denoted a and an outer diameter b, with pressures p_1 and p_2 on its inner and outer surfaces, respectively. It is assumed that only small elastic deformation occurs in the shell, and the mechanical

properties of the shell material satisfy the isotropic assumption. According to the theory of elastic mechanics, the radial stress, tangential stress and radial displacement inside the shell are respectively as follows:

$$\sigma_{\mathrm{r}} = \frac{1}{b^3 - a^3}\left[a^3 p_1 - b^3 p_2 - \frac{a^3 b^3}{r^3}(p_1 - p_2)\right] \tag{21}$$

$$\sigma_{\mathrm{t}} = \frac{1}{b^3 - a^3}\left[a^3 p_1 - b^3 p_2 + \frac{a^3 b^3}{2r^3}(p_1 - p_2)\right] \tag{22}$$

$$u = r\left[\varphi(a^3 p_1 - b^3 p_2) + \omega\frac{a^3 b^3}{r^3}(p_1 - p_2)\right] \tag{23}$$

where r denotes the radius at any point inside the shell, while φ and ω are constants determined by the mechanical properties of the shell, specifically given by $\varphi = (1-2\nu)/(Eb^3-Ea^3)$ and $\omega = (1+\nu)/(2Eb^3-2Ea^3)$, where E represents the elastic modulus and ν is the Poisson's ratio.

The equivalent stress in the shell is calculated using the Von Mises yield criterion [36], as given by the following equation:

$$\sigma_{\mathrm{eq}} = |\sigma_{\mathrm{t}} - \sigma_{\mathrm{r}}| = \frac{3a^3 b^3(p_1 - p_2)}{2(b^3 - a^3)r^3} \tag{24}$$

By assigning $a = r_{\mathrm{Al}}$, $b = r_{\mathrm{p}}$, $p_1 = P_{\mathrm{S}}$, and $p_2 = P_{\mathrm{a}}$, the equivalent stress of the oxide layer at $r = r_{\mathrm{Al}}$ is derived as follows:

$$\sigma_{\mathrm{eq}} = \frac{3r_{\mathrm{p}}^3(P_{\mathrm{S}} - P_{\mathrm{a}})}{2\left(r_{\mathrm{p}}^3 - r_{\mathrm{Al}}^3\right)} \tag{25}$$

where r_{p} is the particle radius, P_{S} is the contact pressure at the Al-Alumina interface, and P_{a} represents the ambient pressure.

Similarly, by assigning values to the variables (a, b, p_1 and p_2) in Fig. 6(b) and substituting into Eq. (23), the expressions for P_{S} and P_{L} in Fig. 6(a) can be derived. Before the aluminum completely melts, lithium is uniformly distributed within the aluminum core, which is surrounded by an oxide layer. Assuming that $P_{\mathrm{L}} = 0$, the calculation formula for P_{S} can be represented as

$$P_{\mathrm{S}} = \frac{\Delta_1/r_{\mathrm{Al}} + (\varphi_{\mathrm{oxide}} + \omega_{\mathrm{oxide}})r_{\mathrm{p}}^3 P_{\mathrm{a}}}{(\varphi_{\mathrm{oxide}} + \varphi_{\mathrm{Al}})r_{\mathrm{Al}}^3 + \omega_{\mathrm{oxide}}r_{\mathrm{p}}^3} \tag{26}$$

where Δ_1 is the total deformation of the Al-Alumina interface. The subscripts oxide and Al denote the oxide layer and aluminum core, respectively.

After the aluminum completely melts, lithium precipitates out of the molten core and forms a spherical droplet within the resulting structure according to the assumption. Similar to Eq. (26), the expressions for P_{S}
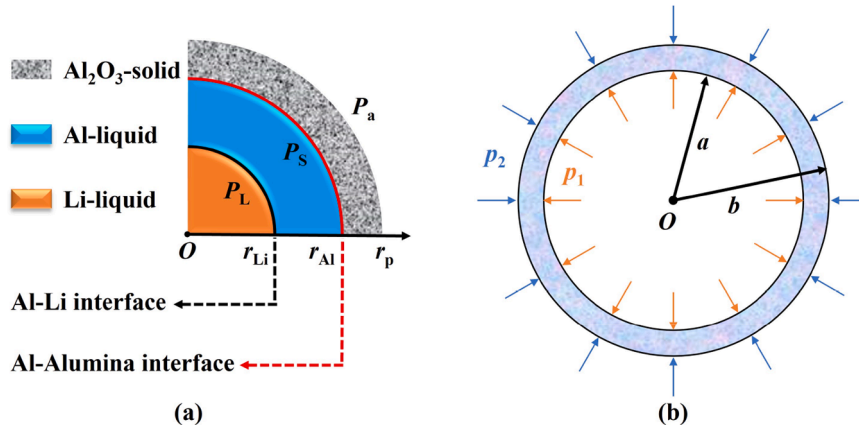

Fig. 6. (a) Schematic of the contact pressure distribution inside the alloy particle. (b) Schematic of a shell subjected to internal and external pressures.

and P_L are given respectively by

$$P_S = \frac{\Delta_1/r_{Al} + (\varphi_{oxide} + \omega_{oxide})r_p^3 P_a + (\varphi_{Al} + \omega_{Al})r_{Li}^3 P_L}{(\varphi_{oxide} + \varphi_{Al})r_{Al}^3 + \omega_{oxide}r_p^3 + \omega_{Al}r_{Li}^3} \tag{27}$$

$$P_L = \frac{\Delta_2/r_{Li} + (\varphi_{Al} + \omega_{Al})r_{Al}^3 P_S}{(\varphi_{Al} + \varphi_{Li})r_{Li}^3 + \omega_{Al}r_{Al}^3} \tag{28}$$

where Δ_2 is the total deformation of the Al-Li interface. The subscript Li denotes the lithium droplet.

After the rupture of the oxide layer, the contact pressure at the Al-Alumina interface decreases to zero, i.e., $P_S = 0$. The pressure on the outer surface of the aluminum core is P_a, and the calculation formula for P_L can be expressed as

$$P_L = \frac{\Delta_2/r_{Li} + (\varphi_{Al} + \omega_{Al})r_{Al}^3 P_a}{(\varphi_{Al} + \varphi_{Li})r_{Li}^3 + \omega_{Al}r_{Al}^3} \tag{29}$$

According to the expressions for P_S and P_L derived above, the contact pressure at the interface depends on its deformation. There are three main factors contributing to the deformation of the Al-Alumina interface [31]: one is the difference in the thermal expansion coefficients between aluminum and alumina; another is the volume change of aluminum during melting; and the last is the volume difference between the formed oxide and the consumed metal in the surface reaction. The deformation at the Al-Li interface is mainly attributed to the difference in the thermal expansion coefficients between aluminum and lithium.

Considering the variation of the thermal expansion coefficient with temperature, the deformations at the Al-Alumina interface and the Al-Li interface, which are caused by the differences in the thermal expansion coefficients, are respectively as

$$\Delta_{1,\alpha} = \sum_i r_{Al,i}(\bar{\alpha}_{Al,i} - \bar{\alpha}_{oxide,i})\delta T_i \tag{30}$$

$$\Delta_{2,\alpha} = \sum_i r_{Li,i}(\bar{\alpha}_{Li,i} - \bar{\alpha}_{Al,i})\delta T_i \tag{31}$$

where $r_{Al,i}$ and $r_{Li,i}$ are the radii of aluminum core and lithium droplet, respectively, $\delta T_i = T_{i+1} - T_i$ represents a small temperature interval, and $\bar{\alpha}_{Al,i}$, $\bar{\alpha}_{Li,i}$ and $\bar{\alpha}_{oxide,i}$ denote the average linear thermal expansion coefficients of aluminum, lithium and alumina, respectively.

The deformation at the Al-Alumina interface caused by aluminum melting is calculated through the following equation:

$$\Delta_{1,melt} = r_{Al,l} - r_{Al,s0} \tag{32}$$

where $r_{Al,s0}$ is the initial radius of the aluminum core, and $r_{Al,l}$ denotes the radius of the molten aluminum core.

In the occurrence of surface reactions, where the stoichiometric ratios between alumina and aluminum, as well as between lithium oxide and lithium, are consistently maintained at 1:2. Therefore, the resultant volume ratio of the oxide formed to the consumed metal can be expressed as

$$\eta = \frac{MW_{oxide}/\rho_{oxide}}{2MW_{metal}/\rho_{metal}} \tag{33}$$

where MW_{oxide} and ρ_{oxide} represent the molar mass and density of the oxide, respectively, while MW_{metal} and ρ_{metal} correspond to the molar mass and density of the metal, respectively.

Then the deformation at the Al-Alumina interface caused by the surface reactions can be calculated by

$$\Delta_{1,hsr} = (\eta - 1)\delta_{Al} \tag{34}$$

where δ_{Al} is the thickness of the aluminum core consumed by the surface reactions.

3.6. Diffusion-controlled combustion

Based on the assumption that the lithium in the alloy particle is completely encapsulated by aluminum during combustion, only the evaporation of aluminum is considered to simplify the combustion model. Furthermore, the combustion process of micron-sized aluminum droplet is generally controlled by diffusion. Considering the slow rate of droplet surface regression, the combustion of aluminum droplet can be characterized as a quasi-steady state process. Assuming a Lewis number of 1, the equations governing mass, species, and energy conservation for this quasi-steady state system, expressed in spherical coordinates, are given as follows [37]:

$$r^2\rho u = \text{Constant} \tag{35}$$

$$r^2\rho u\frac{dY_i}{dr} = \frac{d}{dr}\left(r^2\rho D\frac{dY_i}{dr}\right) + r^2\dot{\Omega}_i \tag{36}$$

$$r^2\rho u\frac{d(c_p T)}{dr} = \frac{d}{dr}\left(r^2\rho D\frac{d(c_p T)}{dr}\right) + r^2\dot{Q} \tag{37}$$

where r, ρ and u correspond respectively to the radius, density, and velocity of any point located above the droplet surface. Y_i and $\dot{\Omega}_i$ are the mass fraction and source term of species i, respectively. c_p and T represent the specific heat capacity and temperature of the gas phase, respectively. D denotes the mass diffusion coefficient, and $\dot{Q}$ accounts for the energy source term due to the gas-phase reaction.

The above three governing equations were solved using a conserved scalar approach, as detailed in Ref. [38]. Consequently, the total mass flow rate can be expressed as

$$\dot{m}_{total} = 4\pi r_{Al,l}\rho D\ln(1+B) \tag{38}$$

where B is the transfer number, its three expressions can be derived from solving Eqs. (35)-(37) as follows:

$$B_{Al-ox} = \frac{-\sum_{ox}\frac{Y_{ox,\infty}}{\kappa_{st,ox}} - Y_{Al,s}}{Y_{Al,s} - f - 1}, ox = O_2, H_2O, CO_2 \tag{39}$$

$$B_{Al-Al_2O_3} = \frac{\frac{Y_{Al_2O_3,\infty}}{\kappa_{st,Al_2O_3}} - Y_{Al,s}}{Y_{Al,s} - \left(1 - \frac{1}{\kappa_{st,Al_2O_3}}\right)f - 1} \tag{40}$$

$$B_{ox-T} = \frac{c_p(T_\infty - T_s) + \sum_{ox}\frac{Y_{ox,\infty}\Delta h_{ox}}{\kappa_{st,ox}}}{(1+f)h_{fg} - \frac{\dot{Q}_{rad} + \dot{Q}_{dep}}{\dot{m}_{total}}}, ox = O_2, H_2O, CO_2 \tag{41}$$

where f is the ratio of the alumina deposition rate to the total mass flow rate, Δh_{ox} is the combustion heat of aluminum vapor in different oxidizers, and $\dot{Q}_{dep}$ represents the energy source term due to the alumina deposition. The subscripts s and ∞ denote the droplet surface and the far field, respectively.

In consideration of the effects of convection and deposited alumina on the aluminum evaporation process, Eq. (38) can be modified as

$$\dot{m}_{total} = 2\pi(1-\beta)r_{Al,l}\rho DSh\ln(1+B) \tag{42}$$

where β represents the fraction of the aluminum core covered by the oxide cap, and is calculated employing the model proposed by King [39].

According to the conservation of mass, the evaporation rate of aluminum and the deposition rate of alumina are given respectively by

$$\dot{m}_{evap} = 2\pi(1+f)(1-\beta)r_{Al,l}\rho DSh\ln(1+B) \tag{43}$$

$$\dot{m}_{dep} = 2\pi f(1-\beta)r_{Al,l}\rho DSh\ln(1+B) \tag{44}$$

4. Results and discussion

4.1. Validation

Based on the sub-models discussed above, a theoretical model was developed to analyze the ignition and combustion characteristics of individual micron-sized Al-Li alloy particle. For validation of the present model, the ignition delay times and critical ignition temperature calculated by the present model were compared with experimental data measured in the reflected shock tube.

Firstly, the ignition process of 8 μm Al-Li alloy particle in air was analyzed by monitoring the temporal variation of particle temperature (T_p) based on the present model. The mass fraction of lithium in the alloy particle was taken as 5 %, and the ambient pressure (P_a) was selected as 5 atm in accordance with the experiment. The ambient temperature (T_a) was gradually increased from 1100 K to determine the critical temperature for particle ignition. For T_a = 1100 K, as plotted in Fig. 7, T_p gradually increases from 298 to 1100 K and remains constant, indicating failure of ignition. The similar phenomenon is observed when T_a is raised to 1300 K. As T_a increases to 1310 K, T_p illustrates a remarkable increase beyond 2327 K, indicating that the particle is successfully ignited. The ignition is also successful when T_a is raised to 1400 K. Therefore, the critical ignition temperature of 8 μm Al-Li alloy particle in air at a pressure of 5 atm predicted by the present model is 1310 K. Subsequently, the reflected shock tube was employed to investigate the ignition characteristics of Al-Li alloy particle at various temperature conditions. During each experiment, P_a was held constant at approximately 5 atm, while T_a was gradually decreased from 2160 K. It was observed that ignition of the Al-Li alloy particle failed when T_a dropped below 1322 K. Thus, the experimentally determined critical ignition temperature stands at 1322 K, demonstrating an excellent alignment with the value predicted by the present model.

Additionally, the ignition delay times measured within the temperature range of 1322 to 2160 K were selected for comparison with predicted results, as illustrated in Fig. 8. The results presented in Fig. 8 demonstrate that the current model is capable of accurately predicting the trend of decreasing ignition delay time of Al-Li alloy particle with increasing T_a.
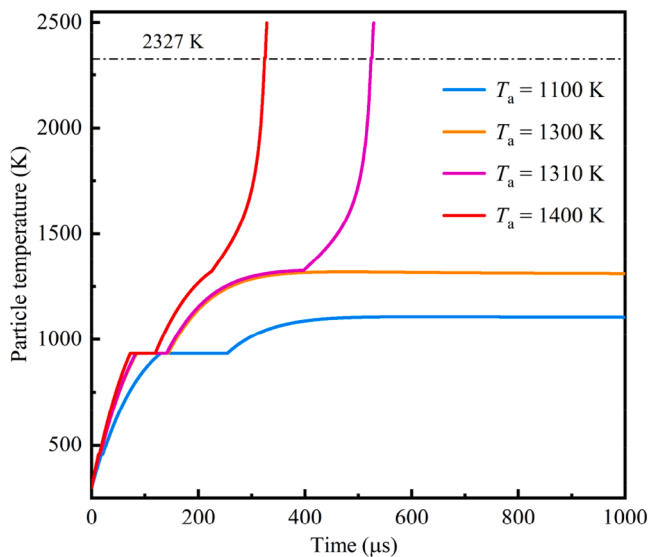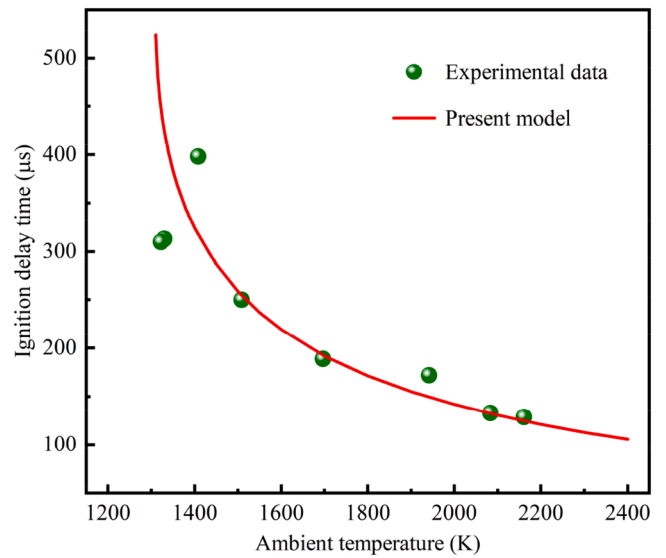

Fig. 8. Comparison of ignition delay times of present model and experimental data.

4.2. Ignition and combustion process analysis
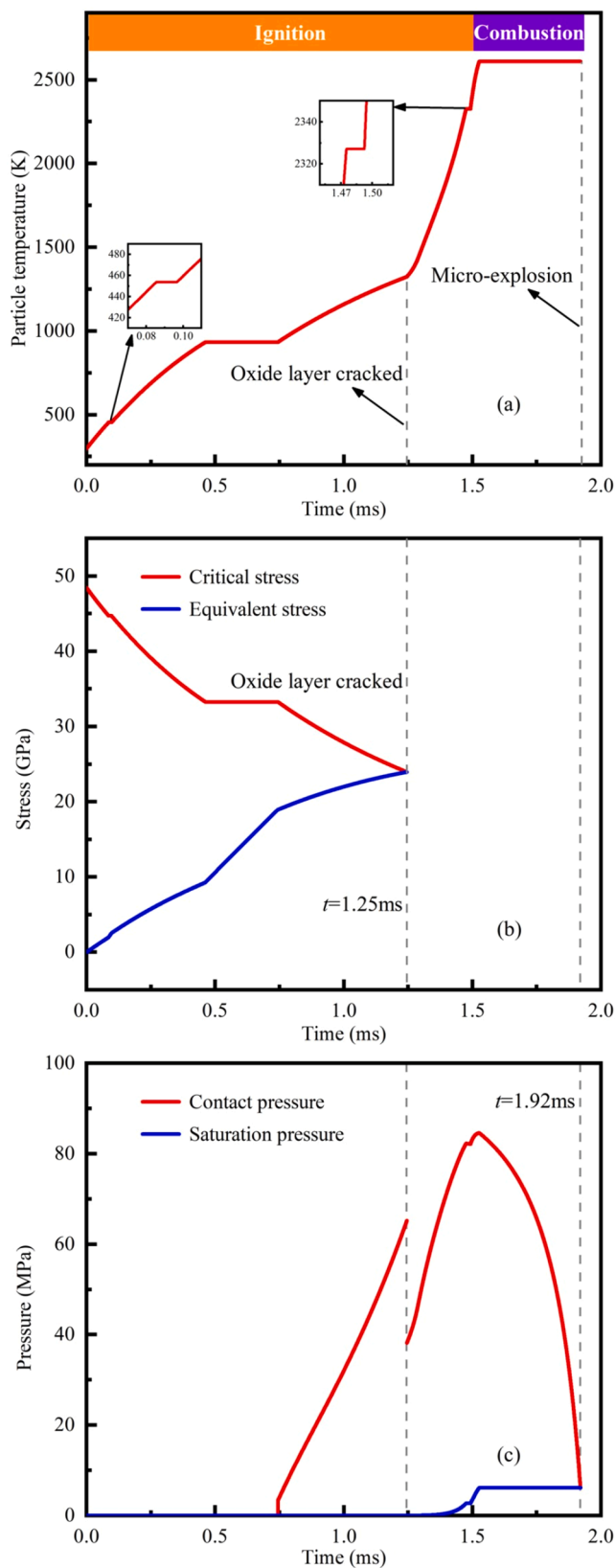
Based on the validated model, the ignition and combustion process of a single 20 μm Al-Li alloy particle containing 5 % lithium was analyzed in this section. The particle was situated in an environment with P_a = 1 atm, T_a = 1500 K, and the following molar fractions: 0.2 for O_2, 0.1 for H_2O, 0.1 for CO_2, and the remaining 0.6 for N_2 as a diluent. The results are presented in Fig. 9, where Fig. 9(a) illustrates the temporal variation of T_p during the ignition and combustion process, Fig. 9(b) shows the variations of critical stress and equivalent stress in the oxide layer, and Fig. 9(c) indicates the variations of contact pressure at the Al-Li interface and saturation vapor pressure of lithium droplet.

It can be observed that, under the combined effects of convective and radiative heat transfer, the temperature of Al-Li alloy particle exposed to high-temperature gas flow gradually increases. Since the LTECs of aluminum and lithium are greater than that of alumina, the Al-Alumina interface undergoes deformation, leading to a gradual increase in equivalent stress within the oxide layer. At t = 0.086 ms, T_p reaches the melting point of lithium, initiating the melting process. Due to the low lithium content, the solid lithium completely melts within 0.01 ms. Subsequently, T_p continues to rise. During the aluminum melting stage, the increase rate in equivalent stress within the oxide layer accelerates significantly, primarily due to volumetric expansion caused by aluminum melting, which exacerbates the deformation at the Al-Alumina interface.

After the complete melting of aluminum, T_p experiences a further increase. Since the LTEC of lithium is greater than that of aluminum, deformation begins to occur at the Al-Li interface, resulting in a rapid increase in contact pressure. At t = 1.25 ms, the equivalent stress within the oxide layer reaches 24 GPa, exceeding the critical stress and leading to the rupture of the oxide layer. Following the rupture, the effective surface area of the aluminum core significantly increases, with exothermic surface reactions becoming the primary heat source for T_p increase, surpassing gas-particle heat transfer. Additionally, due to the loss of restraint from the oxide layer, the pressure on the outer surface of the aluminum core abruptly changes to ambient pressure, causing a sudden drop in contact pressure at the Al-Li interface from 65 MPa before the rupture to 38 MPa after it.

When T_p reaches the melting point of alumina, the oxide layer adhering to the aluminum core's surface rapidly melts. Due to surface tension and gas flow shear force, the molten alumina accumulates on one side of the particle, forming an oxide cap. Consequently, aluminum

Fig. 7. Temperature profiles of Al-Li alloy particle in different ambient temperatures indicating success or failure of ignition.

Fig. 9. (a) Variation of particle temperature during the ignition and combustion process. (b) Variations of critical stress and equivalent stress in the oxide layer. (c) Variations of contact pressure at the Al-Li interface and saturation vapor pressure of lithium droplet (d_p = 20 μm, Y_{Li} = 5 %, P_a = 1 atm, and T_a = 1500 K).

vapor escapes from the exposed aluminum core surface and reacts with surrounding oxidizers. This establishes a diffusion flame above the aluminum droplet surface, marking the transition into a quasi-steady combustion phase. Under the current operating conditions, T_p during combustion stabilizes at 2610 K. This temperature rise from the melting point of alumina to 2610 K occurs within just 0.05 ms, highlighting the rapid transition from ignition to combustion.

During combustion, as aluminum continuously evaporates, the aluminum core covering the lithium droplet progressively thins, causing a gradual reduction in the contact pressure at the Al-Li interface. Since T_p remains constant at 2610 K during the combustion stage, the saturation vapor pressure of lithium remains stable at 6.15 MPa. At t = 1.92 ms, the contact pressure at the Al-Li interface decreases to a level equivalent to the saturation vapor pressure of lithium, triggering instantaneous vaporization of the lithium droplet. The vast volume difference resulting from this vaporization leads to the fragmentation of the aluminum core, a phenomenon known as micro-explosion.

The above calculated results indicate that during the ignition stage, the contact pressure at the Al-Li interface is significantly greater than the saturation vapor pressure of lithium, rendering the micro-explosion of Al-Li alloy particle improbable at this stage. Therefore, micro-explosion can occur as the saturation vapor pressure of lithium exceeds the contact pressure during the combustion stage. As a result, the Al-Li alloy particle first melts, then begins to combust, and finally undergoes micro-explosion due to the significant difference in boiling points between aluminum and lithium. This is consistent with the experimental observations by Terry et al. [18], and Xu et al. [15].

4.3. Parametric study

A parametric study was then conducted to investigate the influences of P_a and T_a on ignition delay time and micro-explosion delay time. As P_a is gradually increased from 1 atm to 80 atm, with all other operating conditions remaining consistent with those described in Section 4.2, the variations in ignition delay time and micro-explosion delay time calculated by the current model as a function of P_a are depicted in Fig. 10. It is evident that both ignition delay time and micro-explosion delay time decrease with increasing P_a. This is because raising P_a enhances gas density, resulting in an increased particle Reynolds number, which in turn accelerates the convective heat transfer rate between the gas and particle. On the other hand, elevated P_a also increases the surface reaction rate to a certain extent, further elevating the particle
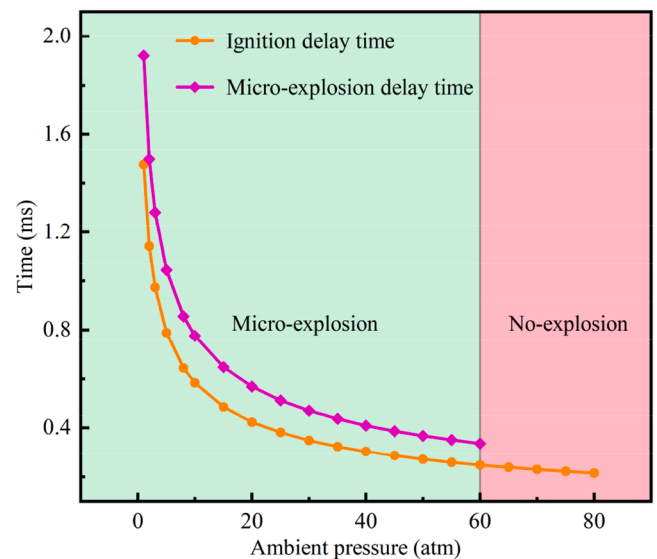
Fig. 10. Variations of ignition delay time and micro-explosion delay time with ambient pressure (d_p = 20 μm, Y_{Li} = 5 %, and T_a = 1500 K).

heating rate and thereby significantly reducing both ignition delay time and micro-explosion delay time.

As P_a increases from 1 to 60 atm, the ignition delay time decreases by 84.4 %, and the micro-explosion delay time decreases by 82.5 %. When P_a exceeds 60 atm, micro-explosion ceases to occur within the Al-Li alloy particle. This is attributed to the fact that the contact pressure at the Al-Li interface consistently remains above the saturation vapor pressure of lithium, preventing the vaporization of lithium droplet and, consequently, failing to meet the conditions for micro-explosion. Therefore, increasing P_a elevates the contact pressure at the Al-Li interface, restricts the vaporization of lithium, and ultimately suppresses the occurrence of micro-explosion in Al-Li alloy particle.

With P_a set at 65 atm and T_a gradually increasing from 1500 to 3800 K, while other operating conditions remain consistent with those described in Section 4.2, the variations of ignition delay time and micro-explosion delay time predicted by the current model with respect to T_a are illustrated in Fig. 11. It is obvious that both ignition delay time and micro-explosion delay time decrease as T_a rises. This can be explained by the significant enhancement of gas-particle heat transfer rates with increased T_a. Furthermore, micro-explosion in Al-Li alloy particle can only occur when T_a exceeds 3000 K. The reason is that higher T_a results in less heat loss of particle during the combustion stage, leading to higher T_p during combustion. According to the Clausius-Clapeyron equation, a higher T_p results in an elevation in the saturation vapor pressure of lithium, which subsequently surpasses the contact pressure at the Al-Li interface, ultimately triggering micro-explosion. Therefore, raising T_a increases the saturation vapor pressure of lithium and promotes the vaporization of lithium droplet, thereby facilitating the occurrence of micro-explosion in Al-Li alloy particle.

The results of the above analysis indicate the existence of a critical ambient pressure (P_{cr}) for a given T_a, under which micro-explosion of Al-Li alloy particle can occur only when P_a is below P_{cr}. Based on the definition of P_{cr}, the present model was employed to calculate P_{cr} for 30–80 μm Al-Li alloy particle with 5 % lithium content at temperatures ranging from 1500 to 3800 K, by maintaining the molar fractions of O_2, H_2O, and CO_2 as 0.2, 0.1, and 0.1, respectively. As illustrated in Fig. 12, P_{cr} rises with an increase in T_a and is independent of particle size. This is because the particle temperature during combustion is primarily controlled by ambient pressure and temperature, exhibiting minimal sensitivity to particle size. The particle temperature variation induced by particle size changes is negligible compared to those caused by
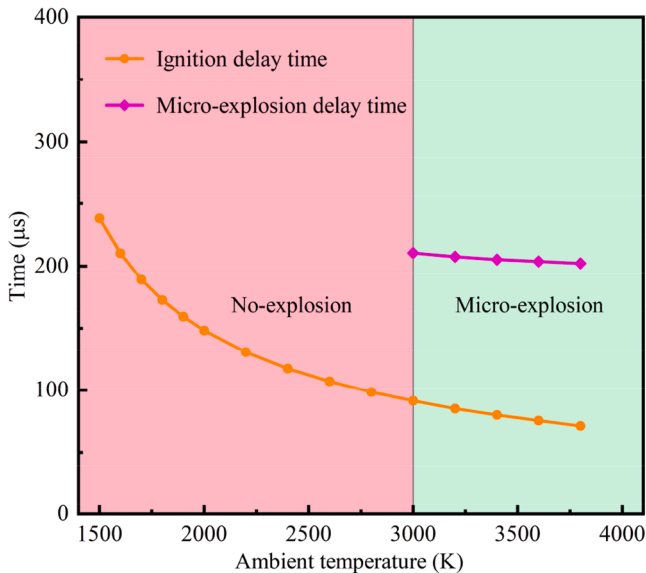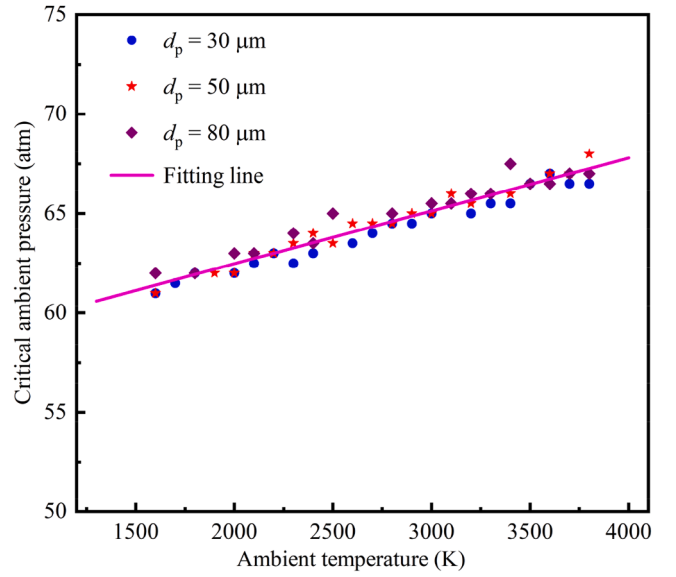

Fig. 12. Variation of critical ambient pressure with ambient temperature.

ambient pressure and temperature, resulting in only minor alterations in the saturated vapor pressure of lithium. Consequently, the effect of particle size on the micro-explosion behavior of alloy particles is weaker than that of ambient pressure and temperature. Linear fitting of the calculated results by using the least squares method yields

$$P_{cr}(\text{atm}) = 57.15 + 0.0027T_a \tag{45}$$

The micro-explosion of Al-Li alloy particle occurs when $P_a \le P_{cr}$, and does not occur when $P_a > P_{cr}$. Experiments conducted by Diez et al. [5] have shown that the agglomerated particle size collected from Al-Li-based propellant burned under 6.89 MPa is significantly larger than that collected under 0.34 MPa. This is attributed to the inhibitory effect of higher pressure on micro-explosion, providing validation of Eq. (45).

5. Conclusions

The present study measured the ignition delay times of Al-Li alloy particle over a wide range of temperatures using a reflected shock tube. Subsequently, theoretical models of ignition and combustion of micron-sized Al-Li alloy particle in high-temperature gas flow were developed. The ignition delay times and critical ignition temperature predicted by the present model are in good agreement with the experimental results. The main conclusions of this study are as follows:

(1) The experimental results show that the ignition delay time of 8 μm Al-Li alloy particle containing 5 % lithium decreases from 310 to 129 μs when the ambient temperature increases from 1322 to 2160 K at a pressure of 5 atm. The critical ignition temperature of such Al-Li alloy particle in air is determined to be 1322 K.
(2) Based on the validated model, a detailed analysis indicates that in the ignition stage, the contact pressure at the Al-Li interface is significantly greater than the saturation vapor pressure of lithium, rendering the micro-explosion of Al-Li alloy particle improbable at this stage. Following the rupture of the oxide layer, the saturation vapor pressure of lithium rapidly rises as a result of the increase in particle temperature. During the combustion stage, the continuous vaporization of aluminum leads to a decrease in the contact pressure at the Al-Li interface. Once the contact pressure drops to a level equivalent to the saturation vapor pressure of lithium, the micro-explosion is triggered.

Fig. 11. Variations of ignition delay time and micro-explosion delay time with ambient temperature (d_p = 20 μm, Y_{Li} = 5 %, and P_a = 65 atm).

(3) A parametric study reveals that increasing the ambient pressure elevates the contact pressure at the Al-Li interface, inhibiting lithium vaporization and thus inhibiting the occurrence of micro-explosion in Al-Li alloy particle. Conversely, raising the ambient temperature increases the saturation vapor pressure of lithium and promotes the vaporization of lithium droplet, thereby facilitating the occurrence of micro-explosion. Furthermore, an expression for the critical ambient pressure at which micro-explosion occurs in Al-Li alloy particle with 5 % lithium content was obtained.

CRediT authorship contribution statement

Zhenkun Hu: Writing – original draft, Validation, Methodology, Investigation, Formal analysis, Data curation. **Shengyu Pang:** Validation, Data curation. **Yugan Liao:** Validation, Methodology. **Yong Tang:** Supervision. **Qian Mao:** Formal analysis. **Baolu Shi:** Writing – review & editing, Project administration, Investigation.

Declaration of competing interest

The authors declare that they have no known competing financial interests or personal relationships that could have appeared to influence the work reported in this paper.

Acknowledgement

References

[1] D.S. Sundaram, P. Puri, V. Yang, A general theory of ignition and combustion of nano- and micron-sized aluminum particles, Combust. Flame 169 (2016) 94–109.
[2] J.K. Sambamurthi, E.W. Price, R.K. Sigman, Aluminum agglomeration in solid-propellant combustion, AIAA J. 22 (1984) 1132–1138.
[3] J. Tang, P. Liu, Guti Huojian Fadongji Yuanli, National Defense Industry Press, Beijing, China, 2013, p. 170.
[4] C. Shen, S. Yan, J. Yao, S. Li, X. Guo, J. Nie, Y. Ou, Q. Jiao, Combustion behavior of composite solid propellant reinforced with Al-based alloy fuel, Mater. Lett. 304 (2021) 130608.
[5] G.A. Diez, T.D. Manship, B.C. Terry, I.E. Gunduz, S.F. Son, Characterization of an aluminum–Lithium-alloy-based composite propellant at elevated pressures, J. Propul. Power 37 (2021) 332–337.
[6] D. Reese, L. Groven, S. Son, A. Mukasyan, Intermetallic Compounds as Fuels for Composite Rocket Propellants, 47th AIAA/ASME/SAE/ASEE Joint Propulsion Conference & Exhibit (2011), pp. AIAA 2011–5865.
[7] Y. Zhu, W. Le, W. Zhao, X. Ma, D. Liu, J. Li, Q. Jiao, Promising fuels for energetics: spherical Al-Li powders with high reactivity via incorporation of Li, Fuel 323 (2022) 124393.
[8] W.M. Lee, R.D. Ford, Reactivity of Al-2.5 pct Li alloy with water as studied by the exploding wire technique, Metall. Trans. B 19 (1988) 255–259.
[9] M. Ahmad, Thermal oxidation behavior of an Al-Li-Cu-Mg-Zr alloy, Metall. Trans. A 18 (1987) 681–689.
[10] A.W. Blackman, D.K. Kuehl, Use of binary light metal mixtures and alloys as additives for solid propellants, ARS J. 31 (1961) 1265–1272.
[11] L. Liu, W. Zhang, W. Xiong, P. Liu, G. He, W. Ao, Investigation of Al-Li particle ignition dynamics with different Li content, Combust. Flame 270 (2024) 113734.
[12] J.T. Moore, S.R. Turns, R.A. Yetter, Combustion of lithium–Aluminum alloys, Combust. Sci. Technol. 177 (2006) 627–669.
[13] J. Tang, P. Liu, Guti Huojian Fadongji Yuanli, National Defense Industry Press, Beijing, China, 2013, p. 43.
[14] M.D. Ruesch, G.C. Mathews, R.J. Tancin, S.F. Son, C.S. Goldenstein, Wavelength-modulation spectroscopy in the mid-infrared for temperature and HCl measurements in aluminum-lithium composite-propellant flames, Combust. Flame 242 (2022) 112180.
[15] D. Xu, S. Li, X. Jin, X. Huang, H. Li, F. Wang, Comparison on the ignition and combustion characteristics of single Al-Li alloy and Al fuel microparticles in air, Combust. Flame 258 (2023) 113114.
[16] X. Zhou, L. Huang, X. Liu, H. Yu, Combustion characteristics of Al-Li alloy powder and its application in solid propellant, J. Phys. 2478 (2023) 032067.
[17] W. Xiong, Y. Liu, T. Zhang, S. Wu, D. Zeng, X. Guo, A. Pang, Effect of Al–Li alloy on the combustion performance of AP/RDX/Al/HTPB propellant, Aerospace 10 (2023) 222.
[18] B.C. Terry, I.E. Gunduz, M.A. Pfeil, T.R. Sippel, S.F. Son, A mechanism for shattering microexplosions and dispersive boiling phenomena in aluminum–lithium alloy based solid propellant, Proc. Combust. Inst. 36 (2017) 2309–2316.
[19] B.C. Terry, T.R. Sippel, M.A. Pfeil, I.E. Gunduz, S.F. Son, Removing hydrochloric acid exhaust products from high performance solid rocket propellant using aluminum-lithium alloy, J. Hazard. Mater. 317 (2016) 259–266.
[20] D. Xu, F. Wang, S. Li, X. Huang, H. Li, Y. Guo, Laser-induced ignition and combustion of single micron-sized Al-Li alloy particles in high pressure air/N2, Aerospace 10 (2023) 299.
[21] Y. Zhou, Q. Mao, S.I. NG, Q. Chu, L. Liao, B. Shi, Fundamental investigation on the micro-explosion of aluminum-lithium alloy particle, Combust. Flame 274 (2025) 113983.
[22] A. Zhang, Y. Li, Thermal conductivity of aluminum alloys—A review, Materials (Basel) 16 (2023).
[23] H.W. Davison, Compilation of Thermophysical Properties of Liquid Lithium, NASA Technical Note, 1968.
[24] J. Zhang, O.T. Stein, T.D. Luu, A. Shamooni, Z. Xia, Z. Luo, L. Ma, Y. Feng, A. Kronenburg, Detailed modeling of aluminum particle combustion – From single particles to cloud combustion in Bunsen flames, Chin. J. Aeronaut. 35 (2022) 319–332.
[25] P.M. Reynolds, Spectral emissivity of 99.7% aluminium between 200 and 540°C, Br. J. Appl. Phys. 12 (2002) 111–114.
[26] J. Zhang, Z. Xia, O.T. Stein, L. Ma, F. Li, Y. Feng, Z. Zhang, A. Kronenburg, Combustion characteristics of aluminum particle jet flames in a hot co-flow, Chem. Eng. J. 442 (2022) 135876.
[27] M. Schiemann, J. Bergthorson, P. Fischer, V. Scherer, D. Taroata, G. Schmid, A review on lithium combustion, Appl. Energy 162 (2016) 948–965.
[28] M.A. Gurevich, G.E. Ozerova, A.M. Stepanov, Heterogeneous ignition of an aluminum particle in oxygen and water vapor, Combust. Explos. 6 (1970) 291–297.
[29] S. Mohan, L. Furet, E.L. Dreizin, Aluminum particle ignition in different oxidizing environments, Combust. Flame 157 (2010) 1356–1363.
[30] X. Mi, A. Fujinawa, J.M. Bergthorson, A quantitative analysis of the ignition characteristics of fine iron particles, Combust. Flame 240 (2022) 112011.
[31] V. Rosenband, Thermo-mechanical aspects of the heterogeneous ignition of metals, Combust. Flame 137 (2004) 366–375.
[32] S.S. Sazhin, O. Rybdylova, C. Crua, M. Heikal, M.A. Ismael, Z. Nissar, A.R.B.A. Aziz, A simple model for puffing/micro-explosions in water-fuel emulsion droplets, Int. J. Heat Mass Transf. 131 (2019) 815–821.
[33] S.V. Stankus, R.A. Khairulin, A.G. Mozgovoi, Experimental study of density and thermal expansion of the advanced materials and heat transfer agents for liquid metal systems of thermonuclear reactor: lithium, High Temp. 49 (2011) 187–192.
[34] R.G. Munro, Evaluated material properties for a sintered alpha-Alumina, J. Am. Ceram. Soc. 80 (1997) 1919–1928.
[35] A.J.C. Wilson, The thermal expansion of aluminium from 0° to 650°C, Proc. Phys. Soc. 53 (1941) 235–244.
[36] M. Kholdi, A. Loghman, H. Ashrafi, M. Arefi, Analysis of thick-walled spherical shells subjected to external pressure: elastoplastic and residual stress analysis, Proc. Inst. Mech. Eng. Pt. L-J. Mater.-Design Appl. 234 (2019) 186–197.
[37] K.K. Kuo, Principles of Combustion, Wiley-Interscience, Hoboken, New Jersey, 2005, pp. 569–581.
[38] P.E. DesJardin, J.D. Felske, M.D. Carrara, Mechanistic model for aluminum particle ignition and combustion in air, J. Propul. Power 21 (2005) 478–485.
[39] M.K. King, Aluminum combustion in a solid rocket motor environment, Proc. Combust. Inst. 32 (2009) 2107–2114.